PAPER

Check for updates

Asymmetric design of a Pt/C catalyst layer for enhanced performance in proton exchange membrane fuel cells

Jinqi Li, [ID] [ab] Weikang Zhu, [ID] *[ab] Yuankai Shao,[ab] Bingjie Zhou,[ab] Shuoyao Yin,[ab] Xiaowei Wang,*[b] Zhenguo Li*[ab] and Yan Yan[b]

The physicochemical properties of catalysts significantly influence the overall performance of proton exchange membrane fuel cells (PEMFCs). However, the complexity arising from numerous interrelated parameters presents significant challenges in establishing comprehensive structure–performance relationships for advanced PEMFC systems. This study systematically evaluates three commercial Pt/C catalysts with distinct morphology and structural characteristics to reveal their specific functional impacts on fuel cell performance. The results indicate the abundant micropores and small-sized Pt nanoparticles, embedded in micropores, can significantly enhance the catalytic performance at the cathode side. Conversely, hydrogen oxidation reaction (HOR), at the anode side, prefers to occur on the surface-active site of carbon support. Furthermore, an asymmetric membrane electrode assembly configuration incorporating optimized catalysts and gas diffusion layer achieves a maximum power density of 2.52 W cm^{-2} (200 kPa absolute pressure with H$_2$ and O$_2$ supplying) with good stability, attributed to synergistic improvements in active site utilization and the mass transfer process. This work enhances the fundamental understanding of catalyst microstructure-performance correlations while offering practical insights for Pt/C catalyst selection and electrode architecture design in PEMFC applications.

Introduction

As an environmentally friendly power source, proton exchange membrane fuel cells (PEMFCs) have been recognized as promising candidates for the next-generation transportation systems with growing market adoption.[1,2] Despite their technological advancements, PEMFCs continue to encounter significant technical barriers, particularly poor durability, low stack performance, and high fabrication cost.[3] According to the DOE Hydrogen Program Record, the stack cost for heavy-duty vehicles (HDV) has been reduced to $99 per kW$_{net}$ under annual production scales of 100 000 systems. However, the prohibitive manufacturing costs of Pt-based catalysts, which contribute 61% of the total fuel cell system cost, remain a critical barrier to achieving further cost reductions in fuel cell technologies. To expedite the commercialization of PEMFCs, innovative catalysts and cost-optimized membrane electrode assembly (MEA) designs with enhanced electrochemical performance are urgently required to meet the scalability requirements of

hydrogen-powered fuel cell electric vehicles (FCEVs).[1] Typically, the membrane electrode assembly (MEA) is conventionally configured with a proton exchange membrane (PEM) sandwiched between paired catalyst layers (CLs) and gas diffusion layers (GDLs). Over the past decades, systematic research endeavors have been directed toward elucidating the critical determinants of PEMFC performance, spanning core component optimization, such as the PEM,[4,5] catalyst, CL,[6–8] GDL,[9–12] bipolar plates,[13–15] as well as advanced fabrication methodologies.[16,17]

During the operation of PEMFCs, H$_2$ and O$_2$ react in the three-phase boundary (TPB) within the anode and cathode CLs, respectively. At the anode, hydrogen oxidation reaction (HOR) proceeds along H$_2 \rightarrow 2H^+ + 2e^-$. The electrons generated at the anode are transported to the cathode *via* the external circuit, while the H$^+$ is concurrently transported through PEM. At the cathode, the oxygen reduction reaction (ORR) predominantly occurs in the cathode catalyst layer, proceeding along $1/2O_2 + 2H^+ + 2e^- \rightarrow H_2O$.[18–20] From a theoretical perspective, the optimal performance characteristics of PEMFCs are contingent upon the synergistic interplay of efficient ORR and HOR processes within the MEA. Consequently, catalysts are recognized as pivotal determinants of both performance and durability, primarily by facilitating multiphase transport and establishing unique TPBs for electrochemical reactions.[21] To

[a]National Engineering Laboratory for Mobile Source Emission Control Technology, China Automotive Technology & Research Center Co., Ltd, Tianjin 300300, China. E-mail: lizhenguo@catarc.ac.cn; zhuweikang@catarc.ac.cn

[b]CATARC Automotive Research and Inspection Center (Tianjin) Co., Ltd, Tianjin, 300300, China. E-mail: wangxiaowei@catarc.ac.cn

qualify as a viable electrocatalyst candidate for PEMFCs, the materials must demonstrate three critical attributes: (1) exceptional electrochemical activity toward ORR and HOR kinetics,[22] (2) substantial electrochemical surface area (ECSA) to maximize TPBs,[23] and (3) optimized electronic conductivity to facilitate charge transfer across catalyst–support interfaces.[24]

In recent years, an increasing number of researchers have realized the importance of directional catalyst design for HOR and ORR application, as well as the asymmetrical catalyst layer architecture for enhanced PEMFC performance. Most importantly, fundamental materials, including catalysts, carbon supports and ionomers, will determine the functionality and performance of CL and PEMFC. Research emphasis on ionomer management has predominantly focused on cathode CLs,[25–27] where controlled adjustment of ionomer content proves effective in balancing power output and durability.[26] Notably, ECSA demonstrates a U-shaped dependence on ionomer loading: inadequate coverage disrupts proton conduction pathways, while excessive amounts induce active site occlusion through ionomer aggregation. Optimal ionomer-to-carbon ratios must account for carbon support porosity characteristics, requiring careful optimization of both ionomer distribution thickness and coverage density.[25,28] Asymmetrical CL configurations enable decoupled optimization of mass transport and charge transfer processes. Anode CLs emphasize enhanced porosity to facilitate hydrogen accessibility and proton conduction, whereas cathode CLs implement graded porosity architectures to simultaneously ensure catalyst utilization and improve water management.[29] Developments in ionomer chemistry and gradient electrode designs further demonstrate potential to minimize oxygen transport resistance through porous media while preventing anode performance decay from excessive ionomer coverage.[30–32]

To further explain the intrinsic relationship between the micro-structure of the catalyst and the mass transfer efficiency, as well as enhance the performance of PEMFC, this work has systematically evaluated three commercial Pt/C catalysts with identical Pt mass loading and different porous structures. The electrochemical behavior of these catalysts was carefully characterized through both RDE and MEA testing technologies to identify the optimal structure of Pt-based catalysts for PEMFC anode and cathode catalyst layer materials. Additionally, an asymmetric MEA with different anode and cathode catalysts was fabricated. The *in situ* electrochemical impedance spectroscopy (EIS) confirmed the optimized mass transfer process and enhanced PEMFC performance, revealing the dominant factors for high-performance PEMFC design.

Experimental

Electrode preparation and MEA fabrication

The Pt/C catalysts employed in this work were commercially available from Premetek (40 wt% Pt on Vulcan XC-72), Johnson Matthey (Hispec 4000), and TANAKA (TEC10E40E) with identical nominal Pt loading of 40 wt%. The standard catalyst ink formulation for RDE tests comprises 5 mg of Pt/C catalyst, 230 μL of ultrapure water, 730 μL of isopropanol, and 40 μL of

Nafion ionomer solution (5 wt%). Following 1 h of ultrasonic treatment, specific quantity of catalyst ink was uniformly deposited onto a clean glassy carbon electrode (5 mm diameter, 0.196 cm²) and subsequently air-dried naturally for use in RDE testing. The catalyst ink formulation for MEA fabrication comprises 48 mg of Pt/C catalyst, 1 mL of ultrapure water, 9 mL of isopropanol, and 411 mg of Nafion ionomer solution (5 wt%). The cathode catalyst inks were spray-coated onto a clean Gore® 12 μm proton exchange membrane at 80 °C. A high-precision electronic balance (Mettler-Toledo XPE, 0.01 mg readability) was employed to measure the mass of the membrane before and after catalyst spraying. The Pt loading of different MEAs is calculated by gravimetry and controlled at 0.2 mg cm^{-2} for cathode catalyst layer. A carbon-fiber-paper-based GDL (220 μm in thickness, with micropore layer) was utilized on the cathode sides of the MEA. In order to investigate the influence of the ionomer/carbon (I/C) ratio, three catalyst inks (I/C = 0.71, 0.56, 0.42) were used to fabricate the cathode catalyst layer with same method. The anode catalyst ink was spray-coated onto the microporous layer (MPL) side of GDL at 80 °C with a Pt loading of 0.1 mg cm^{-2} and an active area of 2×2 cm². The catalyst-coated substrate was sandwiched between the catalyst-coated membrane and cathode gas diffusion layer to assemble the MEA for single-fuel-cell testing. To investigate the influence of GDL, the catalyst layers for both the cathode and anode were prepared *via* the catalyst-coated membrane (CCM) method, which promotes tight catalyst-membrane contact. Two types of GDLs, SGL 22BB (with MPL) and Toray-060 (without MPL), were selected as the GDLs for both anode and cathode during fuel cell testing.

Material characterization

The microstructural morphology and aggregation behavior of catalyst particles were characterized using scanning electron microscope (SEM, Thermo Scientific Apreo S) at a magnification of 50 000×. Additionally, transmission electron microscope (TEM, JEOL JEM-F200) was utilized to evaluate the spatial distribution and nanoscale particle size of Pt deposited on the carbon support. Semi-quantitative analysis of the samples was performed *via* X-ray photoelectron spectrometer (XPS, Thermo Scientific K-Alpha) to determine elemental composition, chemical states, and compositional variations, with results calibrated against the C 1s peak at 284.8 eV. Furthermore, nitrogen physisorption experiments were conducted using a surface area and porosity analyzer (Micromeritics ASAP 2460) at −195.8 °C. The hydrophobicity of the CLs and GDLs was quantified using contact angle goniometry (SINDIN SDC-200S).

RDE testing

Electrochemical measurements were conducted using a standard three-electrode configuration with a CHI760E workstation. A graphite rod, a saturated calomel electrode (SCE), and a catalyst-coated glassy carbon rotating disk electrode (RDE, Pine Research Instrumentation) were employed as the counter electrode, reference electrode, and working electrode, respectively. The electrochemical measurements were performed in an

acidic electrolyte containing 0.1 M $HClO_4$ solution. Prior to linear sweep voltammetry (LSV), all electrodes were electrochemically activated *via* cyclic voltammetry (CV) using a scan rate of 100 mV s^{-1}. LSV measurements for the ORR and HOR were performed using a rotating disk electrode operated at 1600 rpm, with a potential sweep rate of 10 mV s^{-1} from negative to positive potentials. The electrochemical surface area (ECSA, cm^2 mg$_{Pt}^{-1}$) of Pt was determined from the RDE data using the following equation.[33]

$$ECSA = \frac{Q_H}{C \times M} \qquad (1)$$

where, Q_H (μC cm^{-2}) corresponds to the integrated charge density collected in the hydrogen adsorption region, C (210 μC cm^{-2}) is the charge density for a monolayer proton reduction on Pt surface and M (mg cm^{-2}) denotes the Pt mass loading.

PEMFC test

The MEAs were assembled within a single fuel cell equipped with single-channel serpentine flow fields in both bipolar graphite plates. Prior to PEMFC performance evaluation, electrochemical conditioning was conducted with fully humidified H_2 (0.3 slpm) and air (0.5 slpm) under a constant current density of 1 A cm^{-2} (4 A over 2×2 cm^2 active area) with a dwell time of 3 h. A constant reactant flow rate of H_2 (0.3 slpm)–O_2 (0.5 slpm) or H_2 (0.3 slpm)–air (1.5 slpm) was delivered to the anode and cathode sides, respectively, under fully humidified conditions (100% RH) at 80 °C and 200 kPa absolute pressure. Electrochemical impedance spectroscopy (EIS) was performed using Solartron ModuLab XM ECS system to characterize the impedance characteristics of MEAs across a frequency range of 100 kHz to 0.1 Hz, with an applied perturbation amplitude of 0.05 A cm^{-2} or 0.1 A cm^{-2}. For ECSA tests, the anode and cathode were preconditioned with fully humidified H_2 (0.3 slpm) and N_2 (0.5 slpm) under ambient pressure conditions. The ECSA values of the MEAs were quantified *via* CV testing at a scan rate of 200 mV s^{-1} within a potential window of 0.1–1.2 V.

Results and discussion

Physicochemical characterization

To enhance the generalizability, three representative commercial Pt/C catalysts, Premetek 40 wt% on Vulcan XC-72, Johnson Matthey 40 wt% Hispec 4000, and TANAKA 40 wt% Pt/C (denoted as PMK, JM, TKK), were selected to investigate structure–performance relationship for PEMFC application. As the main site for electrochemical reaction, the morphologies of Pt nanoparticles of different catalysts were first observed *via* TEM, as shown in Fig. 1. Pt nanoparticles of PMK (Fig. 1a) and JM (Fig. 1b) are more likely to distribute on the surface of carbon support. On the contrary, uniform Pt nanoparticles can be observed in all the regions of TKK carbon support (as shown in Fig. 1c), suggesting the incorporation of Pt nanoparticles within the micro/mesopores architecture of the carbon support.[34] Meanwhile, the mean particle diameters exhibit notable variations among the catalysts (insets in Fig. 1a to c). The TKK

catalyst exhibits the smallest Pt nanoparticles, with the mean particle size (MPS) of 2.49 ± 0.43 nm. This value progressively increases to 3.36 ± 0.42 nm for the JM catalyst and 3.69 ± 0.50 nm for the PMK catalyst, respectively. In high-resolution TEM images, the distinct lattice fringes can be observed for all the catalysts (Fig. 1d to f). The lattice distance of 0.199 nm, 0.228 nm can be attributed to the (100) and (111) lattice plane of Pt, indicating the high degree of crystallinity.

The SEM images of all the catalysts are shown in Fig. 2a to c. In contrast to the PMK and JM catalysts, the TKK catalyst exhibits significantly smaller carbon particles with uniform spatial distribution across the observed field of view. The high-resolution SEM images (Fig. S1) confirm that the mean carbon particle size of TKK is about 58.9 nm. The small carbon particles of TKK can form uniform secondary porous structures and smooth catalyst layer surface, which may lead to the larger electrochemically active surface area and higher electrochemical performance. To quantitatively investigate the pores of different catalysts, the nitrogen adsorption–desorption isotherms and corresponding pore size distribution curves are analyzed. All the samples show similar isotherm types, as shown in Fig. 2d. Compared with PMK and JM catalysts, TKK exhibits observably high adsorption capacity in low P/P_0 region. Meanwhile, a noticeable hysteresis loop can be observed in the region of $0.4 < P/P_0 < 0.8$, indicating the hierarchical pore structure of TKK catalyst with abundant micropores and a small amount of mesopores.[35,36] The above conclusion is confirmed by the pore size distribution analysis by nonlocal density functional theory (NLDFT) method (Fig. 2e). A large number of micropores can be observed within the micropore range of TKK catalyst, resulting in the highest micropore volume (0.114 cm^3 g^{-1}, Table S1). For all catalysts, the proportion of mesoporous volume (2–50 nm) is the largest, which may derive from the inter-particle accumulation effect of carbon support. As shown in Fig. 2f, the total pore volume of TKK can reach 0.598 cm^3 g^{-1}, which is about 2-fold than that of other catalysts. Due to the abundance of micropores and mesopores, the specific surface area of TKK, analyzed by Brunauer–Emmett–Teller (BET) method, has reached 395.45 m^2 g^{-1}, which is double that of PMK (141.54 m^2 g^{-1}) and JM (151.57 m^2 g^{-1}) catalysts, implying the adequate sites for Pt nanoparticles loading.

X-ray photoelectron spectroscopy (XPS) was employed to characterize the chemical states of Pt across the catalysts. The surface Pt concentration of the TKK catalyst (2.13 at%) is relatively lower than that of PMK (3.33 at%) and JM (4.22 at%) catalysts. As shown in Fig. 3a, the XPS spectra of Pt 4f can be deconvoluted into two sets of peaks, attached to Pt^0 and Pt^{2+} species. Across all three catalysts, metallic Pt (Pt^0) is the dominant species (>85%, Fig. 3b), which may facilitate exposure of active sites for ORR and HOR process, resulting in enhanced catalytic activity.[37,38] To reveal the distribution of elements along the radial direction in different Pt/C catalysts, the depth-profiling XPS analysis coupled with argon-ion etching was conducted. The whole etching protocol comprises four stages with each etching depth of about 10 nm. As a whole, the types of elements in different catalysts are similar (Fig. S2). However, from surface to bulk, the proportions of Pt, C and O show
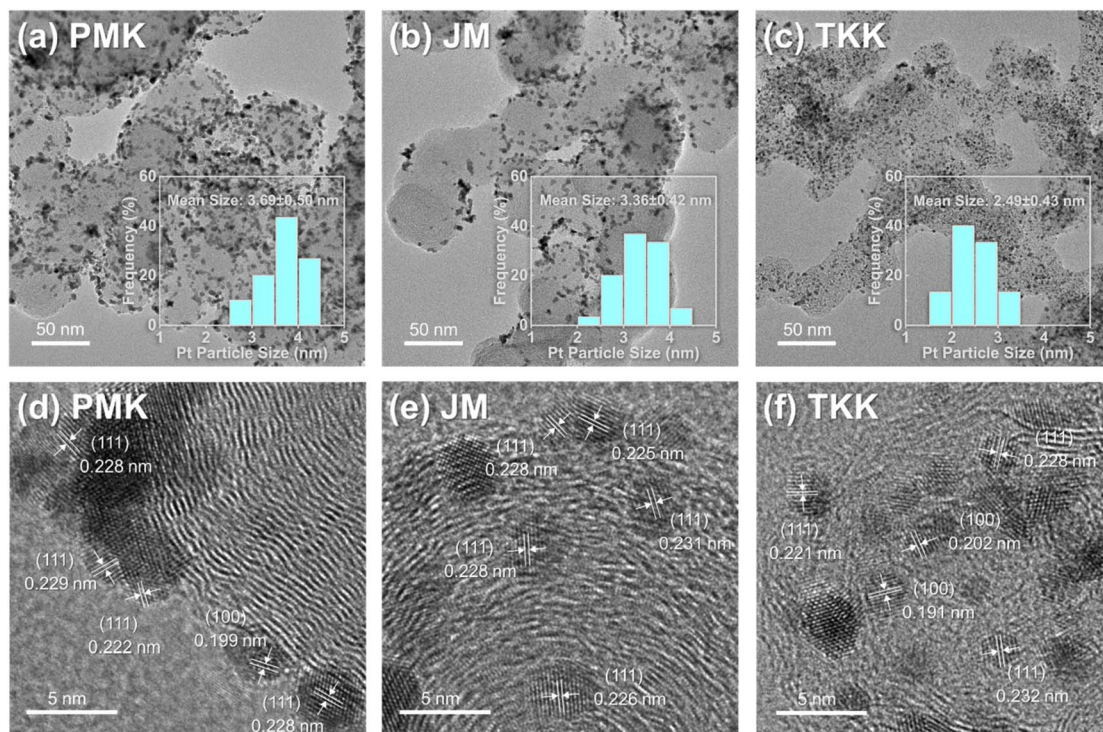
Fig. 1 The morphology of different Pt-based catalysts. The TEM images of (a) PMK, (b) JM and (c) TKK catalysts. The inset is the corresponding particle size distribution histogram. The HR-TEM images of (d) PMK, (e) JM and (f) TKK catalysts.

obvious change (Fig. 3c). As the gradual exposure of internal structure of catalyst particles, the Pt proportions of JM and PMK catalysts exhibit a downward trend with fluctuation. Conversely, the Pt proportion of TKK catalyst gradually increases from 2.13 at% to 2.99 at%, indicating that compared with the PMK and JM

catalysts, there might be some ultrafine Pt nanoparticles embedded within the carbon support of the TKK catalyst. Combined with the pore size distribution analysis of TKK catalyst, the Pt nanoparticles may be preferentially embedded in the micropores of carbon support. It is worth noting that the C
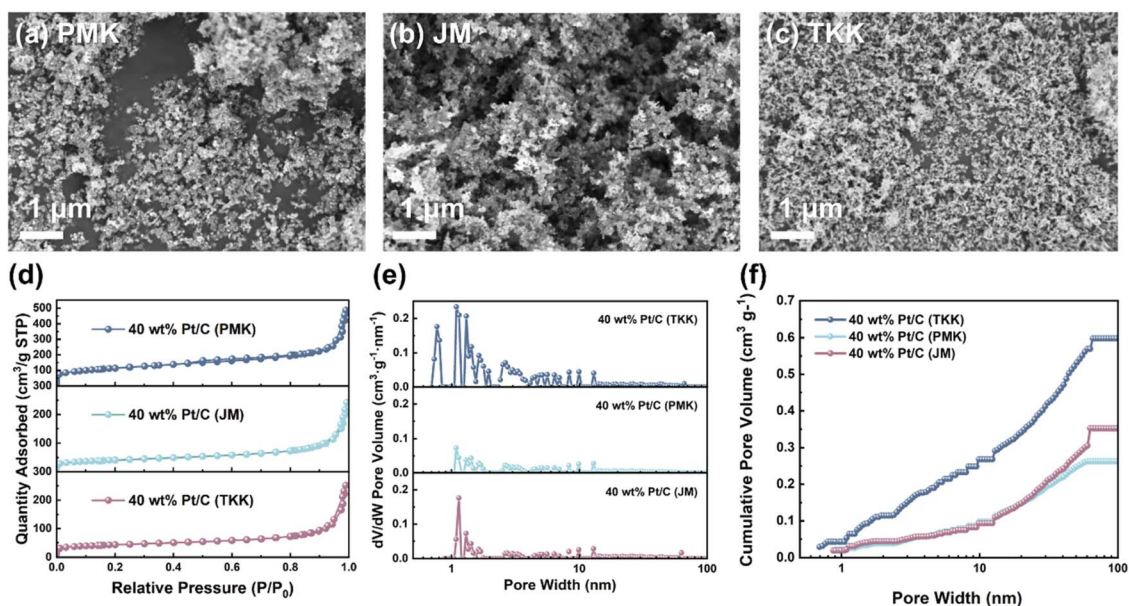

Fig. 2 The micro-structure analysis of different Pt/C catalysts. The SEM morphology of (a) PMK, (b) JM and (c) TKK catalysts. (d) The nitrogen adsorption–desorption isotherms and corresponding (e) pore size distribution curves simulated by NLDFT method. (f) The cumulative pore volume of different catalysts.
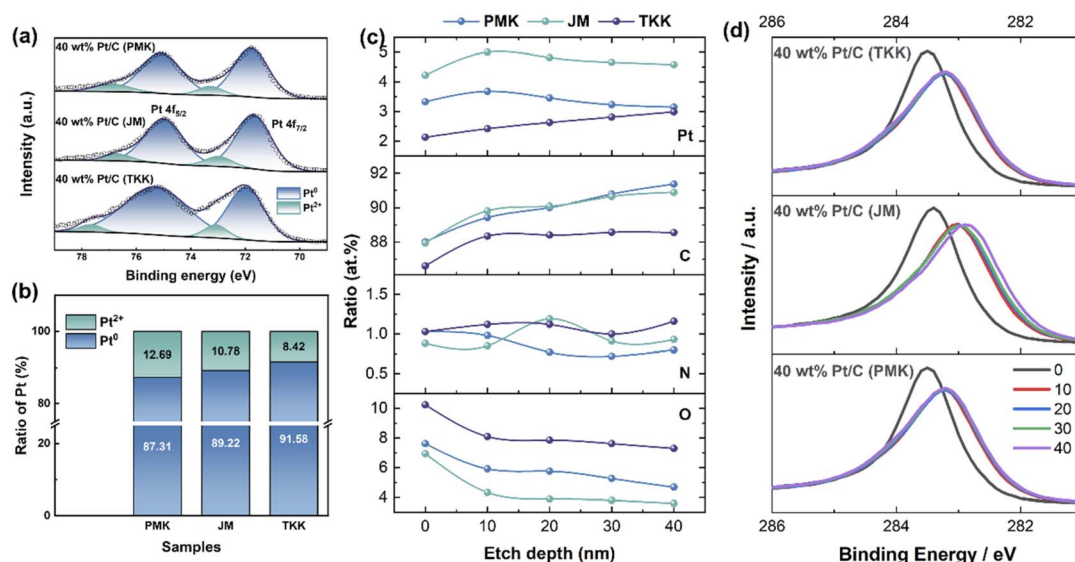
Fig. 3 The chemical state and element analysis of different Pt/C catalysts. (a) The XPS Pt 4f spectra and corresponding deconvoluted curves. (b) The histogram of Pt^{2+} and Pt^0 species on the surface of different Pt/C catalysts. The (c) elements content curves and (d) C 1s spectra of the Pt/C catalysts derived from XPS analysis with argon ion etching.

and O distribution along the radial direction shows completely opposite trends. The surface of the catalyst is more prone to oxidation, leading to the higher content of O. As the elements on the catalyst surface were etched, the percentage of O elements rapidly decreased, as shown in Fig. S3. The high resolution XPS spectra of Pt 4f (Fig. S4) indicates the relatively stable chemical state of Pt atoms from surface to inside of catalyst particles. By contrast, with continuous argon ion etching, C 1s peak positions of all the catalysts shift to lower binding energy (Fig. 3d), indicating most C atoms are oxidized on carbon particle surface, which also verifies the analysis of O 1s XPS. Through a persuasive XPS analysis, it can be seen that the distribution of Pt elements in the TKK catalyst is significantly different, compared with JM and PMK. The Pt nanoparticles are more likely to be detected inside the carbon support. Meanwhile, over 91.5% of the Pt elements exist in Pt^0 species.

RDE test

This study first employed the RDE method to investigate the intrinsic activities of the three catalysts for the oxygen reduction reaction (ORR) at the cathode and the hydrogen oxidation reaction (HOR) at the anode. As shown in Fig. 4a, TKK catalyst demonstrates a notable positive shift in LSV curve, compared with PMK and JM catalysts, indicating the higher intrinsic activity of ORR.[39] As a quantitative index, TKK catalyst exhibits higher half-wave potentials ($E_{1/2}$) of 0.888 V versus RHE, compared to PMK (0.837 V versus RHE) and JM (0.856 V versus RHE) catalysts. The TKK catalyst also shows impressive mass activity (MA) and specific activity (SA) of 44.4 $\mu A\ \mu g_{Pt}^{-1}$ and 134.8 $\mu A\ cm_{Pt}^{-2}$ at 0.9 V versus RHE, respectively. Meanwhile, the electrochemical surface area (ECSA, as shown in Table 1)

increases from 32.9 $m^2\ g_{Pt}^{-1}$ for PMK and 38.0 $m^2\ g_{Pt}^{-1}$ for JM to 66.8 $m^2\ g_{Pt}^{-1}$ for TKK catalyst, as shown in Fig. 4b and d. The Tafel plot in Fig. 4c shows the smaller slope value of 77.9 mV dec^{-1} for the TKK catalyst, significantly lower than those of the PMK (89.9 mV dec^{-1}) and JM (82.7 mV dec^{-1}) catalysts, suggesting higher ORR kinetic activity. All the RDE results suggest that TKK catalyst demonstrates superior ORR activity, positioning it as a promising candidate for PEMFC cathode applications. Fig. 4e displays the HOR polarization curves for the PMK, JM and TKK catalysts. The limiting current density slightly increases from 0.558 mA cm^{-2} for JM catalyst to 0.577 mA cm^{-2} for PMK catalyst and finally to 0.671 mA cm^{-2} for TKK catalyst. In Fig. 4f, all the catalysts also exhibit almost overlapped Tafel curves, indicating the similar catalytic activities to HOR process. Therefore, TKK catalyst seems to be the best candidate for PEMFC. The superior catalytic performance may be attributed to two synergistic structural advantages: (1) the substantial micro/mesopores architecture of the TKK carbon support provides a large surface area for active site loading and electrochemical reaction. (2) The spatial confinement of micropores can reduce the diameter of Pt nanoparticles, thereby maximizing ECSA and generating abundant active sites for catalyst performance enhancement.

Symmetric MEA design

After RDE test, these catalysts were also used to fabricate the MEAs (identical catalyst in both cathode and anode) to investigate the real performance during PEMFC application. The MEAs fabricated using PMK, JM and TKK catalysts were respectively designated as PMK/PMK, JM/JM and TKK/TKK. Unexpectedly, the TKK-based MEA exhibits the worst PEMFC performance (Fig. 5a). PMK- and JM-based MEAs show the
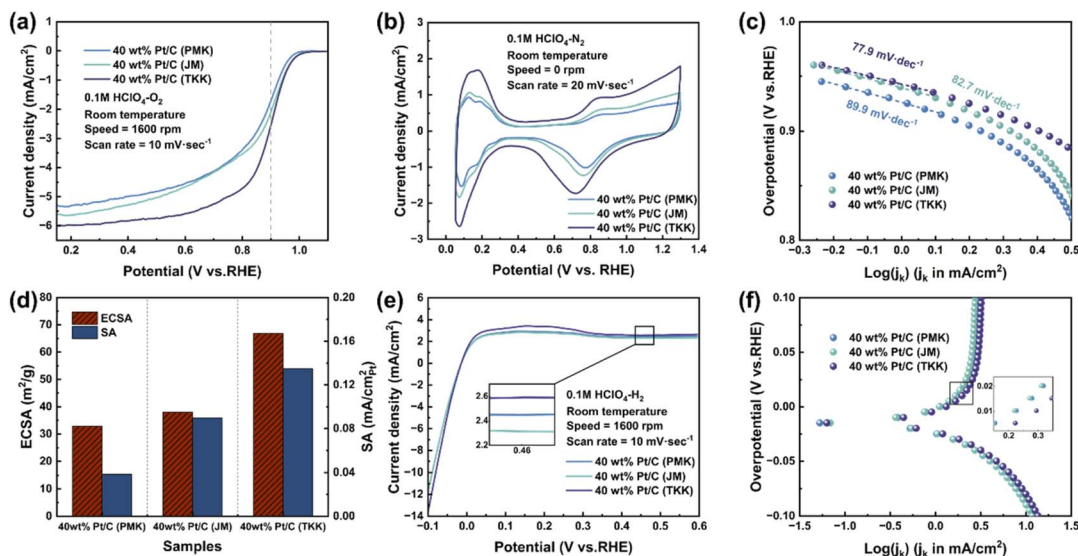
Fig. 4 The electrochemical activity of different catalysts *via* RDE tests. The ORR (a) LSV curves at 1600 rpm with scanning rate is 10 mV s^{-1}, (b) CV curves under N$_2$ atmosphere with scanning rate is 20 mV s^{-1}. (c) Tafel plots of different catalysts derived from LSV curves. (d) The ECSA and SA values of ORR. The HOR (e) LSV curves at 1600 rpm with scanning rate is 10 mV s^{-1} and corresponding (f) Tafel plots.

comparable fuel cell performance in the low-current region (0–1.0 A cm^{-2}). As the increase of current density, the PMK-based MEA exhibits enhanced power density, which can be attributed to the reduced mass-transport-related losses. Under O$_2$ supplying conditions, the polarization curves of MEAs were further validated to demonstrate the superior performance of PMK-based MEA. As shown in Fig. 5b, the PMK/PMK achieved a current density of 57.4 mA cm^{-2} at 0.9 V under H$_2$–O$_2$ conditions exhibiting much higher maximum power density of 1.94 W cm^{-2}, compared with JM/JM (1.76 W cm^{-2}) and TKK/TKK (1.15 W cm^{-2}). To reflect realistic operating conditions, the power densities at 0.7 V under H$_2$–air and H$_2$–O$_2$ conditions were compared, as listed in Table S3. The JM/JM achieved much higher maximum power density of 1.21 W cm^{-2} at 0.7 V under H$_2$–O$_2$ conditions, compared with PMK/PMK (1.08 W cm^{-2}) and TKK/TKK (0.72 W cm^{-2}). It's worth noting that, compared with RDE measurements, the actual fuel cell performance of the TKK-based MEA shows significant attenuation. To elucidate the underlying mechanisms, the *in situ* electrochemical characteristics including ECSA and electrochemical impedance spectroscopy (EIS) of different MEAs were conducted during fuel cell testing. As shown in Fig. 5c, under N$_2$ atmosphere in cathode, the CV curves of all PEMFCs are recorded at the potential range of 0.1–1.2 V with scan rate of 200 mV s^{-1}. The ECSA values derived from CV curves of different MEAs show the similar trends with RDE measurements. The TKK-based MEA exhibited

the highest ECSA (75.3 m^2 g$_{Pt}^{-1}$), approximately double the value compared to the PMK-based (38.3 m^2 g$_{Pt}^{-1}$) and JM-based (33.7 m^2 g$_{Pt}^{-1}$) MEAs. It is worth noting that as the decrease of relative humidity in fuel cell, the value of ECSA shows a significant decline for all the MEAs, as shown in Fig. S5. However, TKK-based MEA still demonstrated the largest electrochemical active area, even under the dry gas condition. TKK catalyst with smaller Pt nanoparticles can provide larger Pt surface and three-phase boundary (TPB) for electrochemical reaction. In EIS Nyquist plots, the ohmic resistance (R_Ω) and charge transfer resistances at the anode (R_{ct1}) and cathode (R_{ct2}) were systematically compared (as shown in Fig. 5d). As established in prior analyses, ORR at the cathode side is more challenging compared to HOR at the anode, thus leading to larger semicircle in low-frequency region (R_{ct2}). Notably, in addition to R_{ct2}, another semicircle is discernible in the high-frequency region (>1000.0 Hz), corresponding to the anode charge transfer resistance (R_{ct1}). The impedance values derived from Nyquist plots are summarized in Table 2. It is worth noting that there are significant differences compared with RDE test. PMK/PMK and JM/JM exhibit much smaller anode charge transfer resistance (R_{ct1}). However, R_{ct1} rapidly increases to 59.30 mΩ for TKK/TKK MEA, which is more than three times that of R_{ct1} of other MEAs. The hydrophobicity of all the MEAs were also systematically evaluated through water contact angle measurements to investigate the anti-flooding capability. As shown in

Table 1 The key parameters for ORR of different catalysts *via* RDE tests

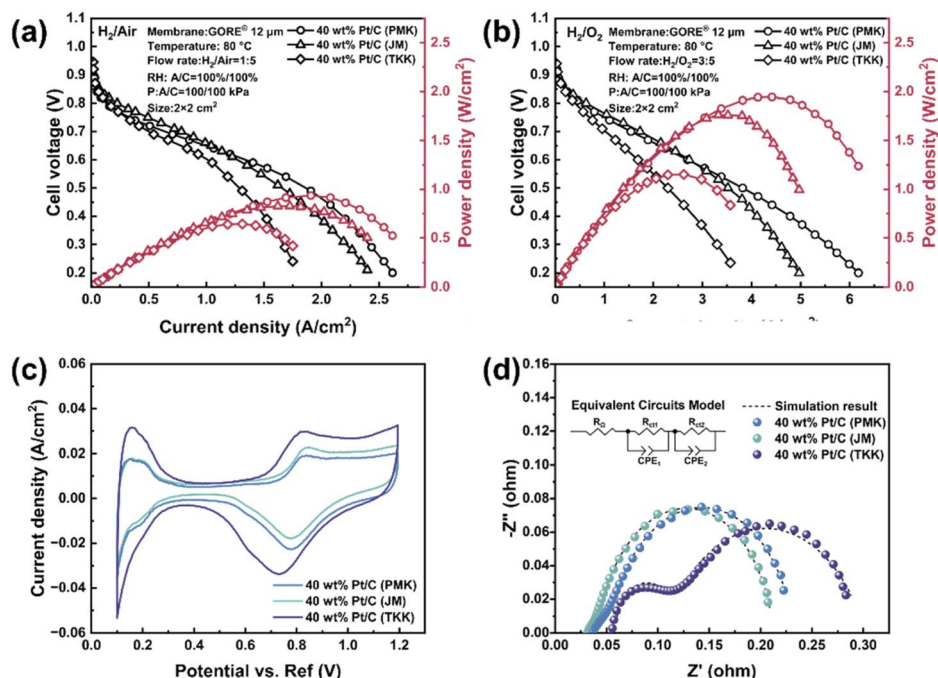| Samples	ECSA (m^2 g$_{Pt}^{-1}$)	j_L (mA cm^{-2})	$j_{0.9\ V}$ (mA cm^{-2})	MA (μA μg$_{Pt}^{-1}$)	SA (μA cm$_{Pt}^{-2}$)
PMK	32.9	5.36	1.71	25.6	38.3
JM	38.0	5.66	2.10	34.1	89.6
TKK	66.8	6.12	2.55	44.4	134.8

Fig. 5 The PEMFC performance of the symmetrical MEA with same catalyst in both cathode and anode. The polarization curves of different MEAs under 200 kPa absolute pressure at 80 °C with (a) H_2–air and (b) H_2–O_2 supplying. The PEMFC tests of (c) ECSA curves, (d) EIS Nyquist plots (@0.1 A cm^{-2}, inset is the corresponding equivalent circuit model[42]).

Table 2 The impedance parameters derived from EIS fitting of different MEAs

Anode/cathode	R_Ω (mΩ)	R_{ct1} (mΩ)	R_{ct2} (mΩ)
PMK/PMK	38.56	18.36	175.11
JM/JM	32.98	12.69	166.29
TKK/TKK	49.63	59.30	171.53
JM/PMK	37.94	10.39	175.58
JM/JM	32.98	12.69	166.29
JM/TKK	27.97	11.73	145.20
PMK/TKK	27.48	9.80	164.14
JM/TKK	27.97	11.73	145.20
TKK/TKK	49.63	59.30	171.53

Fig. S6 and Table S2, all the catalyst layers show obvious hydrophobicity and similar values of contact angle. As is well known, insufficient water retention resulting from excessive catalyst layer hydrophobicity may reduce proton exchange membrane conductivity, while water flooding due to pore blockage at reactive interfaces induces mass transport limitations and consequent PEMFC performance degradation.[40] Notwithstanding, TKK catalyst has the biggest ECSA value and shows higher HOR and ORR activities during RDE tests, PMK/PMK and JM/JM MEAs exhibit the better performance in PEMFC, which may due to the different active sites distribution and carbon support structure. The above conclusion further emphasizes the completely different reaction processes of anode and cathode catalyst layers. Therefore, different characteristics of catalysts, including porous structure and active site

distribution, need to be carefully considered for high PEMFC performance.[41]

Asymmetric MEA design

To further optimize the overall performance of fuel cell, asymmetric MEAs were designed by employing different catalysts in cathode and anode catalyst layers. Firstly, the JM catalyst was employed as anode catalyst, while PMK, JM and TKK catalysts were utilized as cathode catalysts, designated as JM/PMK, JM/JM, JM/TKK, respectively. The EIS Nyquist plots of above MEAs, which were acquired at 0.1 A cm^{-2}, are compiled in Fig. S7a. Only a semi-circle can be observed, belonging to the charge transfer resistance of cathode. In low current density region (0.1 A cm^{-2}), JM/TKK shows the smallest charge transfer resistance of 145.20 mΩ, indicating superior catalytic activity, compared with other MEAs. In the high current density region (1.5 A cm^{-2}, see Fig. S7b), the performance of JM/TKK may be restricted. The polarization curves obtained under air supplying corroborate the aforementioned conclusion, as shown in Fig. 6a. From 0 to 1.5 A cm^{-2}, JM/TKK exhibits higher power density attributed to its abundant micropores and large ECSA. However, under high current density condition (>1.5 A cm^{-2}), the structural characteristic of micropore will lead to negative impacts on the fuel cell performance due to the degenerative mass transfer efficiency. Although the JM/JM exhibits a slightly higher power density (1.21 W cm^{-2}, seen in Fig. S8) at 0.7 V under H_2–O_2 supplying, compared with JM/TKK (1.20 W cm^{-2}) and JM/PMK (0.96 W cm^{-2}), the JM/TKK achieves the highest maximum power density of 2.13 W cm^{-2} under the same
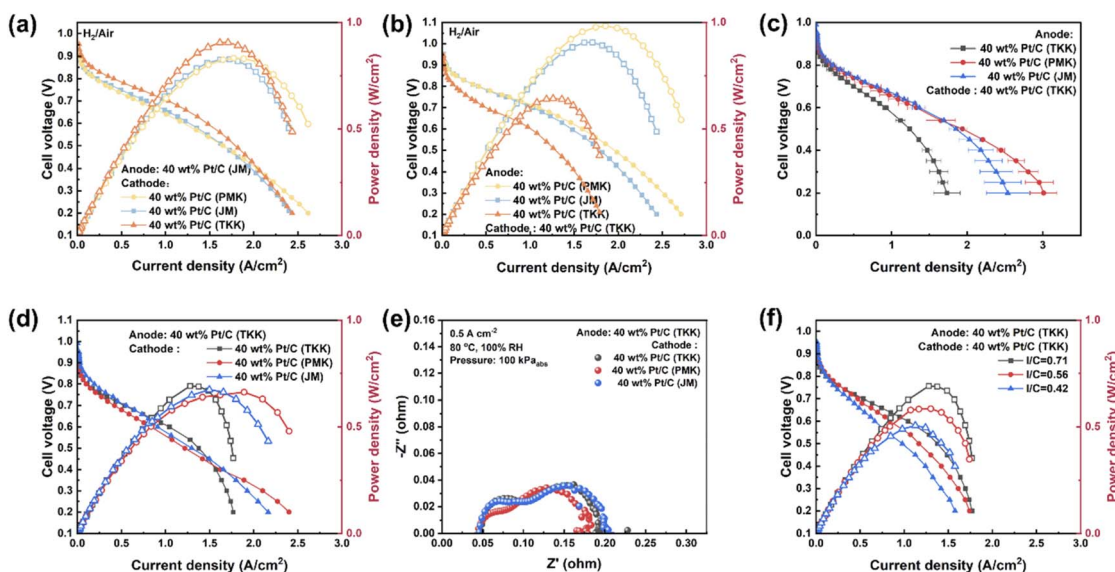
Fig. 6 The PEMFC performance of the asymmetrical MEA with different catalysts in cathode and anode. Polarization curves of MEAs under H_2–air supplying with different (a) cathode catalysts and (b) anode catalysts. (c) The polarization curves of the MEAs with error bars. Polarization curves under H_2–air supplying of (d) the MEAs with TKK as the anode catalyst and corresponding (e) EIS Nyquist plots. (f) The polarization curves of TKK-based MEAs with different I/C values.

condition, as listed in Table S3. This disparity suggests that TKK exhibits higher catalytic activity towards ORR particularly under oxygen-rich operating conditions. The superior performance of the TKK-based cathode catalyst is predominantly governed by the smallest Pt nanoparticle size and maximized electrochemical active area. The abundant porosity and increased active sites of TKK-based MEA facilitate the establishment of large TPBs, thereby enhancing proton and electron transport. This structural advantage is primarily attributed to the reduction of R_{ct2} in the TKK-based MEA. Under H_2–O_2 supplying condition, the JM/PMK, JM/JM and JM/TKK demonstrate analogous behavioral profiles, when the current density is less than 3 A cm^{-2}. However, a pronounced decline in power density is detected for both JM/JM and JM/PMK MEAs in the concentration polarization region, which may stem from their inadequate specific surface area and ECSA values. On the contrary, TKK-based cathode catalyst layer shows alleviative attenuation due to the adequate active sites for ORR, leading to efficient mass transfer and better fuel cell performance.

Fig. 6b shows the polarization curves of MEAs with the fixed TKK-based cathode catalyst layer and different anode catalysts. The corresponding EIS Nyquist plots of all the MEAs under 0.1 A cm^{-2} and 0.5 A cm^{-2} are exhibited in Fig. S9. As quantitatively analyzed in Table 2, the TKK/TKK exhibits a larger charge transfer resistance, reaching 59.30 mΩ, which is 6.05-fold and 5.06-fold those of PMK/TKK and JM/TKK, respectively. This pronounced disparity in charge transfer resistance serves as a principal determinant of the performance constraints in the PEMFCs. As shown in Fig. S8b, the power densities at 0.7 V for the MEAs exhibit a decline under H_2–O_2 supplying condition, from 1.34 W cm^{-2} for PMK/TKK to 0.72 W cm^{-2} for TKK/TKK. The maximum power densities for the MEAs exhibit

a consistent trend, from 2.52 W cm^{-2} for PMK/TKK to 1.15 W cm^{-2} for TKK/TKK. Compared with the RDE test of TKK catalyst (Fig. 4e), the fuel cell performance of TKK-based MEA (Fig. 6b) significantly decreased. Repetitive experiments were conducted to verify the reliability of the above conclusion, as shown in Fig. 6c. In the low current density region, the data shows good repeatability. On the contrary, in the large current density region, the data fluctuates significantly. Nevertheless, the MEA with TKK as the anode catalyst still exhibited poorer fuel cell performance. Furthermore, MEAs with TKK catalyst as the anode and different catalysts as the cathode were fabricated and carried out the electrochemical test (Fig. 6d and e). Relatively low power density and large charge transfer resistance of all the samples provide convincing evidence. It is worth noting that the non-negligible internal resistance does not originate from the excessively high content of polymers. As the ionomer/carbon (I/C) ratio decreases in Fig. 6f, the performance of the fuel cell further decreases, suggesting that the optimal I/C value for TKK-based catalyst layer is 0.71.

Due to the dense structure of the MEA, water diffusion within the membrane electrode (both catalyst layer and GDL) is prone to be hindered under high current density. Considering that there are numerous microporous structures in the TKK catalyst, which may be blocked by water under high current density, the Pt nanoparticles embedded in micropores are difficult to participate in the electrochemical reaction. To verify the above hypothesis, we used hydrophobic carbon fiber paper (Toray 060-10%PTFE, denoted as CFP-060) as the GDL for TKK-based MEA, as shown in Fig. 7. Compared with the traditional GDL (Fig. 7a and b), CFP-060 (Fig. 7c and d) does not have a micropore layer, which may accelerate the transport of water and gas. Under H_2–air supplying the maximum power density of
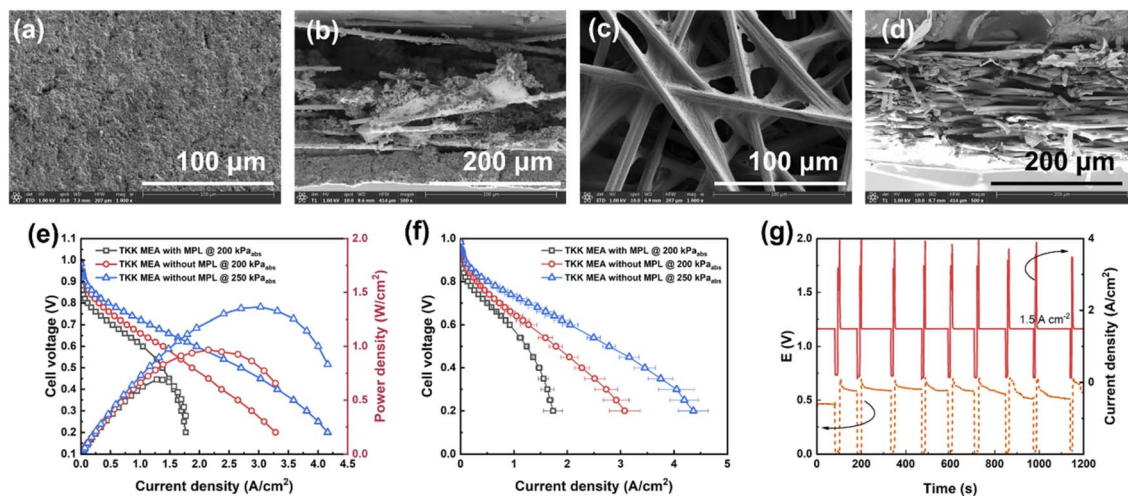
Fig. 7 Structure and performance analysis of TKK-based MEA with different gas diffusion layers. The surface and cross-sectional morphology of (a) and (b) GDL with MPL and (c) and (d) GDL without MPL. (e) The polarization curves of TKK-based MEAs and (f) the corresponding polarization curves with error bars. (g) The stability curves of TKK-based MEA without MPL.

CFP-060 based MEA can reach 0.97 W cm^{-2}, which can further increase to 1.36 W cm^{-2} with the pressure increase to 250 kPa$_{abs}$ (Fig. 7e). This significant improvement in the performance of the fuel cell might be attributed to the extremely high activity of TKK catalyst and the excellent mass transfer efficiency of the GDL. Unfortunately, this excellent performance is accompanied by significant instability as shown in Fig. 7f. Under the galvanostatic method condition (1.5 A cm^{-2}), a dramatic degradation occurs every 100 s, which may be due to the accumulation and elimination of water within the MEA. On the contrary, the Pt nanoparticles on the carbon support surface (such as PMK and JM catalysts) show relatively higher stability, due to the high accessibility, large TPB and efficient mass transfer in catalyst layer. Whether under H$_2$–O$_2$ supplying or H$_2$–air supplying, PMK/TKK demonstrates superior fuel cell performance, suggesting the asymmetric MEA design with PMK and TKK catalysts, as anode and cathode catalyst respectively, can significantly enhance the mass transfer efficiency and the utilization of active metals.

As the primary sites for electrochemical reaction and mass transfer process, the microstructure of catalyst material has a significant impact on the overall performance of fuel cell. As for cathode side, small Pt nanoparticles, obtained from the spatial confinement effect of micropore-rich carbon support, can provide large ECSA and TPB, leading to optimized ORR kinetics. Meanwhile, the secondary pore structure, which is formed by highly dispersed carbon particle during the spraying process, enhances the mass transfer process of oxygen in the cathode catalyst layer. Therefore, the TKK catalyst, which combines small Pt particle, large specific surface area and a highly dispersed carbon support, exhibits excellent performance in fuel cells. On the anode side, due to the extremely rapid kinetics of the HOR, the Pt nanoparticles, which are distributed on carbon support surface, can significantly reduce mass transfer resistance, leading to higher fuel cell

performance. The Pt nanoparticles, which are confined in micropores exhibit limited accessibility for HOR process, inducing elevated anode charge transfer resistance. As previously elucidated, the HOR and ORR mechanisms exhibit fundamentally distinct characteristics in terms of reaction pathways and kinetic behaviors at the anode and cathode, respectively. Consequently, the large specific surface area and ECSA of the TKK-based cathode catalyst layer serve as a pivotal determinant for the overall performance of the PEMFCs. However, the above advantage will turn into a disadvantage at the anode, resulting in the attenuation of the overall performance of the fuel cell.

Conclusion

This study delivers a systematic evaluation of different Pt/C catalysts to elucidate structure–performance relationship between microstructure and electrochemical performance in PEMFCs. The different performances of the MEAs can be attributed to the diversity of microstructure, chemical composition, and hydrophobicity. Micropore-rich carbon support can provide enough sites for nucleation of Pt nanoparticles, leading to smaller Pt particle size and higher ECSA. Therefore, TKK catalyst exhibits superior ORR activity as cathode catalyst layer material during PEMFC test. In contrast, Pt nanoparticles (PMK catalyst), which are formed on the surface of micropore-poor carbon support, will obviously increase the active site utilization and reduce the mass transfer resistance during anode HOR process. By combining anode micropore-poor Pt/C catalyst (PMK, Pt loading 0.1 mg cm^{-2}) with cathode micropore-rich Pt/C catalyst (TKK, Pt loading 0.2 mg cm^{-2}), high performance PEMFC with the power density of 2.52 W cm^{-2} can be obtained. This study offers valuable insights for screening commercial Pt/C catalyst materials during fuel cell manufacturing processes. Meanwhile, the asymmetrical design of catalyst layer provides a useful reference for MEA structure development. This will

facilitate the coordinated advancement of low-cost and high-performance in fuel cell equipment integration.

Conflicts of interest

The authors declare that they have no known competing financial interests or personal relationships that could have appeared to influence the work reported in this paper.

Data availability

The data supporting this article, including SEM, XPS and electrochemical analysis, have been included as part of the supplementary information (SI). See DOI: https://doi.org/10.1039/d5ra06885a.

Acknowledgements

References

1 B. G. Pollet, S. S. Kocha and I. Staffell, Current status of automotive fuel cells for sustainable transport, *Curr. Opin. Electrochem.*, 2019, **16**, 90–95.

2 F. Işıklı, A. Sürmen and A. Gelen, Modelling and Performance Analysis of an Electric Vehicle Powered by a PEM Fuel Cell on New European Driving Cycle (NEDC), *Arabian J. Sci. Eng.*, 2021, **46**(8), 7597–7609.

3 C. Lee, W. J. M. Kort-Kamp, H. Yu, D. A. Cullen, B. M. Patterson, T. A. Arman, S. Komini Babu, R. Mukundan, R. L. Borup and J. S. Spendelow, Grooved electrodes for high-power-density fuel cells, *Nat. Energy*, 2023, **8**(7), 685–694.

4 P. Guan, Y. Zou, M. Zhang, W. Zhong, J. Xu, J. Lei, H. Ding, W. Feng, F. Liu and Y. Zhang, High-temperature low-humidity proton exchange membrane with "stream-reservoir" ionic channels for high-power-density fuel cells, *Sci. Adv.*, 2023, **9**(17), eadh1386.

5 Y. Choi, P. Platzek, J. Coole, S. Buche and P. Fortin, The Influence of Membrane Thickness and Catalyst Loading on Performance of Proton Exchange Membrane Fuel Cells, *J. Electrochem. Soc.*, 2024, **171**(10), 104507.

6 J. Zhao, H. Liu and X. Li, Structure, Property, and Performance of Catalyst Layers in Proton Exchange Membrane Fuel Cells, *Electrochem. Energy Rev.*, 2023, **6**(1), 13.

7 Y. Guo, F. Pan, W. Chen, Z. Ding, D. Yang, B. Li, P. Ming and C. Zhang, The Controllable Design of Catalyst Inks to Enhance PEMFC Performance: A Review, *Electrochem. Energy Rev.*, 2020, **4**(1), 67–100.

8 H. Li, H. Zhao, B. Tao, G. Xu, S. Gu, G. Wang and H. Chang, Pt-Based Oxygen Reduction Reaction Catalysts in Proton Exchange Membrane Fuel Cells: Controllable Preparation and Structural Design of Catalytic Layer, *Nanomater*, 2022, **12**(23), 4173.

9 H. Chun, D.-H. Kim, H.-S. Jung, J. Sim and C. Pak, Effects of gas-diffusion layer properties on the performance of the cathode for high-temperature polymer electrolyte membrane fuel cell, *Int. J. Hydrogen Energy*, 2023, **48**(71), 27790–27804.

10 C.-J. Tseng and S.-K. Lo, Effects of microstructure characteristics of gas diffusion layer and microporous layer on the performance of PEMFC, *Energy Convers. Manage.*, 2010, **51**(4), 677–684.

11 G. Ren, Z. Qu, X. Wang and G. Zhang, Enhancing the performance of proton exchange membrane fuel cell using nanostructure gas diffusion layers with gradient pore structures, *Int. J. Hydrogen Energy*, 2024, **52**, 1161–1172.

12 F. Cai, S. Cai, S. Li and Z. Tu, Performance Enhancement in Proton Exchange Membrane Fuel Cells with the Grooved Gas Diffusion Layer, *Energy Fuels*, 2024, **38**(19), 19011–19028.

13 T. Wilberforce, A. G. Olabi, D. Monopoli, M. Dassisti, E. T. Sayed and M. A. Abdelkareem, Design optimization of proton exchange membrane fuel cell bipolar plate, *Energy Convers. Manage.*, 2023, **277**, 116586.

14 K. Xiong, W. Wu, S. Wang and L. Zhang, Modeling, design, materials and fabrication of bipolar plates for proton exchange membrane fuel cell: a review, *Appl. Energy*, 2021, **301**, 117443.

15 J. N. Qiao, H. Guo, F. Ye and H. Chen, Performance evaluation of proton exchange membrane fuel cells adopting rectangular-baffle and tapered flow channels with an equivalent average depth, *Int. J. Hydrogen Energy*, 2024, **21**(13), 3023–3039.

16 K. Song, Y. Wang, Y. Ding, H. Xu, P. Mueller-Welt, T. Stuermlinger, K. Bause, C. Ehrmann, H. W. Weinmann, J. Schaefer, *et al.*, Assembly techniques for proton exchange membrane fuel cell stack: a literature review, *Renewable Sustainable Energy Rev.*, 2022, **153**, 111777.

17 P. Lin, P. Zhou and C. W. Wu, A high efficient assembly technique for large PEMFC stacks, *J. Power Sources*, 2009, **194**(1), 381–390.

18 T. A. M. Suter, K. Smith, J. Hack, L. Rasha, Z. Rana, G. M. A. Angel, P. R. Shearing, T. S. Miller and D. J. L. Brett, Engineering Catalyst Layers for Next-Generation Polymer Electrolyte Fuel Cells: A Review of Design, Materials, and Methods, *Adv. Energy Mater.*, 2021, **11**(37), 2101025.

19 N. Alonso-Vante, Parameters Affecting the Fuel Cell Reactions on Platinum Bimetallic Nanostructures, *Electrochem. Energy Rev.*, 2023, **6**(1), 3.

20 M. M. Tellez-Cruz, J. Escorihuela, O. Solorza-Feria and V. Compañ, Proton Exchange Membrane Fuel Cells (PEMFCs): Advances and Challenges, *Polymers*, 2021, **13**(18), 3064.

21 S. Jiang, Q. Xiang, Z. Xie, N. Yang, J. Liu, L. Li and Z. Wei, Influence of the Pt/ionomer/water interface on the oxygen reduction reaction: insights into the micro-three-phase interface, *Chem. Sci.*, 2024, **15**(46), 19290–19298.

22 Y. Li, X. Zhu, Y. Chen, S. Zhang, J. Li and J. Liu, Rapid synthesis of highly active Pt/C catalysts with various metal loadings from single batch platinum colloid, *J. Energy Chem.*, 2020, **47**, 138–145.

23 M. M. Rahman, K. Inaba, G. Batnyagt, M. Saikawa, Y. Kato, R. Awata, B. Delgertsetsega, Y. Kaneta, K. Higashi, T. Uruga, *et al.*, Synthesis of catalysts with fine platinum particles supported by high-surface-area activated carbons and optimization of their catalytic activities for polymer electrolyte fuel cells, *RSC Adv.*, 2021, **11**(33), 20601–20611.

24 F. Zhan, K.-S. Hu, J.-H. Mai, L.-S. Zhang, Z.-G. Zhang, H. He and X.-H. Liu, Recent progress of Pt-based oxygen reduction reaction catalysts for proton exchange membrane fuel cells, *Rare Met.*, 2024, **43**(6), 2444–2468.

25 Q. Xue, R. Zhang, D. Yang, B. Li, P. Ming and C. Zhang, Effect of ionomer content on cathode catalyst layer for PEMFC via molecular dynamics simulations and experiments, *Int. J. Hydrogen Energy*, 2022, **47**(55), 23335–23347.

26 W. Olbrich, T. Kadyk, U. Sauter, M. Eikerling and J. Gostick, Structure and conductivity of ionomer in PEM fuel cell catalyst layers: a model-based analysis, *Sci. Rep.*, 2023, **13**(1), 14127.

27 F. Chen, L. Guo, D. Long, S. Luo, Y. Song, M. Wang, L. Li, S. Chen and Z. Wei, Overcoming the Limitation of Ionomers on Mass Transport and Pt Activity to Achieve High-Performing Membrane Electrode Assembly, *J. Am. Chem. Soc.*, 2024, **146**(44), 30388–30396.

28 A. Kobayashi, T. Fujii, C. Harada, E. Yasumoto, K. Takeda, K. Kakinuma and M. Uchida, Effect of Pt and Ionomer Distribution on Polymer Electrolyte Fuel Cell Performance and Durability, *ACS Appl. Energy Mater.*, 2021, **4**(3), 2307–2317.

29 Y. Zhang, P. Jia, S. Yang, J. Su and L. Guo, Enhancing the performance of proton-exchange membrane fuel cell by optimizing the hydrophobicity and porosity of cathode catalyst layer, *Sci. China: Technol. Sci.*, 2025, **68**(3), 1320101.

30 S. Shahgaldi, A. Ozden, X. Li and F. Hamdullahpur, Cathode catalyst layer design with gradients of ionomer distribution for proton exchange membrane fuel cells, *Energy Convers. Manage.*, 2018, **171**, 1476–1486.

31 X. Huang, Y. He, Y. Sun, L. Sun, T. Wang and X. Zhang, Gradient ionomer designed cathode catalyst layer for proton exchange membrane fuel cells with enhanced performance, *J. Power Sources*, 2024, **603**, 234488.

32 Y. Sun, S. Polani, F. Luo, S. Ott, P. Strasser and F. Dionigi, Advancements in cathode catalyst and cathode layer design for proton exchange membrane fuel cells, *Nat. Commun.*, 2021, **12**(1), 5984.

33 Q. Zhao, T. Morawietz, P. Gazdzicki and K. A. Friedrich, Strategy to tune properties of PEM fuel cell electrodes with low Pt loading based on inkjet printing parameters, *J. Power Sources*, 2025, **625**, 235624.

34 G. S. Harzer, A. Orfanidi, H. El-Sayed, P. Madkikar and H. A. Gasteiger, Tailoring Catalyst Morphology towards High Performance for Low Pt Loaded PEMFC Cathodes, *J. Electrochem. Soc.*, 2018, **165**(10), F770–F779.

35 H. Kang, Y. Liu, D. Li and L. Xu, Study on the Removal of Iron and Manganese from Groundwater Using Modified Manganese Sand Based on Response Surface Methodology, *Appl. Sci.*, 2022, **12**(22), 11798.

36 C. Schlumberger and M. Thommes, Characterization of Hierarchically Ordered Porous Materials by Physisorption and Mercury Porosimetry—A Tutorial Review, *Adv. Mater. Interfaces*, 2021, **8**(4), 2002181.

37 X. Zhao, B. Hui, X. Chen, T. Jia, X. Yu, L. Li, X. Zhang, Z. Lu and X. Yang, ORR properties of PtM (M = Fe and Ni) ordered alloys with the effect of small molecules of cyanamide, *Appl. Surf. Sci.*, 2024, **663**, 160183.

38 X. Gao, S. Dai, Y. Teng, Q. Wang, Z. Zhang, Z. Yang, M. Park, H. Wang, Z. Jia, Y. Wang, *et al.*, Ultra-Efficient and Cost-Effective Platinum Nanomembrane Electrocatalyst for Sustainable Hydrogen Production, *Nano-Micro Lett.*, 2024, **16**(1), 108.

39 H. Wang, Y. Song, Q. Peng, X. Gu, J. Zhang, Y. Zhang, X. Wang, X. Yang and W. Lin, Pt/C Electrocatalysts with High Pt Density: A Case Study on Oxygen Reduction Performance from Rotating Disk Electrode to Membrane Electrode Assembly, *Energy Fuels*, 2024, **38**(8), 7311–7321.

40 H. Ungan and A. Bayrakçeken Yurtcan, PEMFC catalyst layer modification with the addition of different amounts of PDMS polymer in order to improve water management, *Int. J. Energy Res.*, 2019, **43**(11), 5946–5958.

41 T. Lazaridis, B. M. Stühmeier, H. A. Gasteiger and H. A. El-Sayed, Capabilities and limitations of rotating disk electrodes versus membrane electrode assemblies in the investigation of electrocatalysts, *Nat. Catal.*, 2022, **5**(5), 363–373.

42 Z. Zhao, Y. Zou, P. Liu, Z. Lai, L. Wen and Y. Jin, EIS equivalent circuit model prediction using interpretable machine learning and parameter identification using global optimization algorithms, *Electrochim. Acta*, 2022, **418**, 140350.